Finite-element methods for spatially resolved mesoscopic electron transport

Stephan Kramer
Institut für Numerische und Angewandte Mathematik der Universität Göttingen, Lotzestraße 16-18, 37073 Göttingen, Germany
(Received 4 June 2013; revised manuscript received 26 July 2013; published 18 September 2013)

A finite-element method is presented for calculating the quantum conductance of mesoscopic two-dimensional electron devices of complex geometry attached to semi-infinite leads. For computational purposes, the leads must be cut off at some finite length. To avoid spurious, unphysical reflections, this is modeled by transparent boundary conditions. We introduce the Hardy space infinite-element technique from acoustic scattering as a way of setting up transparent boundary conditions for transport computations spanning the range from the quantum mechanical to the quasiclassical regime. These boundary conditions are exact even for wave packets and thus are especially useful in the limit of high energies with many excited modes. Yet, they possess a memory-friendly sparse matrix representation. In addition to unbounded domains, Hardy space elements allow us to truncate those parts of the computational domain which are irrelevant for the calculation of the transport properties. Thus, the computation can be done only on the region that is essential for a physically meaningful simulation of the scattering states. The benefits of the method are demonstrated by three examples. The convergence properties are tested on the transport through a quasi-one-dimensional quantum wire. It is shown that higher-order finite elements considerably improve current conservation and establish the correct phase shift between the real and the imaginary parts of the electron wave function. The Aharonov-Bohm effect demonstrates that characteristic features of quantum interference can be assessed. A simulation of electron magnetic focusing exemplifies the capability of the computational framework to study the crossover from quantum to quasiclassical behavior.

DOI: 10.1103/PhysRevB.88.125308 PACS number(s): 02.70.Dh, 73.23.Ad

I. INTRODUCTION

The theoretical understanding of low-temperature quantum transport in mesoscopic electron devices has been pioneered by Landauer[1] and Büttiker.[2] Their approach allows us to understand the quantum interference in submicron Aharonov-Bohm–(AB–) type geometries,[3,4] quantization of the conductance of point contacts and Hall geometries,[5–7] and other phenomena such as reproducible (universal) conductance fluctuations[8] or signatures of quantum chaos in electron transport through two-dimensional (2D) cavities.[9]

Quantitative calculations of the phenomena have been carried out by using the Landauer relation between zero-temperature direct-current electron conductance and quantum transmission.[10] In practice, this implies that the calculation of the quantum coherent transport requires knowledge of the quantum transmission amplitudes.[11] These can be determined without knowing the space dependence of the wave functions of the scattering states. However, a central result of recent scanning probe microscopy experiments[12–14] is a spatially resolved picture of the electron flow through the two-dimensional electron gas (2DEG) under the condition of stationary current flow. These experimental recordings have revealed caustic phenomena and current branching in absence[13–15] and in presence of magnetic fields.[12]

For a detailed comparison of theory, simulation, and experiment, the computation of the scattering wave functions is mandatory. It is the aim of this work to provide a tool for the accurate prediction of the wave functions of scattering states and the corresponding current densities in semi-infinite systems with complex boundaries.

While a scanning probe microscopy experiment can only give a detailed account of the system including the perturbation due to the charged tip of the microscope, a simulation can assess the properties of the unperturbed system and additionally is able to model the experiments by including the tip as a further contribution to the background potential. The work of Szafran[16] shows that the tip can be accurately modeled as a Lorentzian and it is not necessary to take into account interaction effects. As already done by Aidala,[12] the fringes in the local electron density obtained from the simulation can be used to assess the interaction of the tip and the electron wave.

Neglecting the spin and apart from the electron wavelength, three length scales characterize a 2DEG: the elastic mean-free path due to disorder scattering, the coherence length due to interaction-induced inelastic scattering, and the magnetic length. In the ballistic regime, i.e., on length scales less than the mean-free path between two scattering events, electrons move almost unimpeded. At sufficiently low temperatures, the coherence length due to interaction effects can be made arbitrarily long leaving the elastic mean-free path due to impurities, a material parameter, to set the length scale for the dimensions of a 2DEG device to be ballistic. In such devices, scattering occurs only at the walls and in the contacts.

At low temperatures and for high electron-mobility materials such as GaAs/AlGaAs heterostructures, the elastic mean-free path of an electron can be of the order of several tens of micrometers. Hence, the experimentally observed low-temperature transport in micron-size semiconductor devices can be considered as essentially ballistic. For this special case, the quantum mechanical transport properties can be calculated from the solution of the single-electron Schrödinger equation using an appropriate effective mass in the kinetic energy, a local potential which models the details of the device, and a vector potential in case a magnetic field is applied.

In general, for complex geometries, the Schrödinger equation can not be solved analytically. For the vast majority of potentials and geometries of complicated shape, e.g., an Aharonov-Bohm ring with some realistic contacts, the

Schrödinger equation must be solved numerically by some local discretization technique such as finite differences or finite-element methods (FEM). The former is conceptually simpler in that it just reverts derivatives to the difference quotients they have been derived from. Finite elements have their roots in computational fluid dynamics and provide a well-established theoretical and practical framework for the solution of nonlinear systems of partial differential equations on complex geometries. Special types of finite elements can be shown to be equivalent to particular finite differences. For instance, on a regular Cartesian mesh subdivided into triangles, linear Lagrange elements lead to the same matrix representation of the Laplacian as nearest-neighbor finite differences. The advantage of finite elements is that discretization means integration. This considerably reduces the regularity requirements for the solution of a partial differential equation (PDE) and tremendously simplifies the proper treatment of spatially varying coefficients. The electrostatic potential in the Schrödinger equation is a good example for this, in particular, when it models internal details of the shape of the 2DEG device.

Lent and Kirkner[17] were one of the first to apply finite elements to current-carrying states in mesoscopic samples. The scattering problem for 2D ballistic samples including the effect of a perpendicular magnetic field has been studied by Wang *et al*.[18] and Ueta and Miyagawa.[19] In one dimension (1D), the convergence properties have been studied by Power and Rawitcher.[20] Including electron interaction, FEMs have been adapted to finite-size scaling in three dimensions (3D) and were employed to compute quantum critical parameters for a two-electron atom by Antillon *et al*.[21] Especially for wave functions in the scattering region, the correct choice of boundary conditions at some artificial boundary is essential. It seems that the case where only a subset of the domain of the 2DEG is of physical interest and how the uninteresting part can be properly truncated from the computational domain has not been addressed, yet.

The main contribution of this work is the development of a hybrid finite-element Hardy space infinite-element (HSE) formulation for ballistic electron transport in spatially unbounded 2DEGs. HSE methods have been developed recently to improve transparent boundary conditions (TBC) for FEM for acoustic scattering.[22–24] The particular feature of the HSEs is that they lead to a formally exact TBC even for a multimodal wave function.

Transparent boundaries allow us to truncate the physically uninteresting parts from the 2DEG and the leads thus considerably lowering the computational costs. In the leads, unphysical, spurious reflections must be avoided which otherwise would spoil the measured transport properties. The presentation of the TBC in this work is independent of the spatial dimension and the particular application. Thus, it applies to three-dimensional wave phenomena as well.

In contrast to standard recursive Green's function approaches based on tight-binding models, we use higher-order finite elements on irregular, problem-adapted meshes which in general can not be obtained from Cartesian grids by means of a single coordinate transformation.[25] Moreover, higher-order finite elements significantly reduce numerical dispersion errors.[26,27]

The numerical accuracy of the method is demonstrated by studying the quality of the current conservation in a quasi-one-dimensional (quasi-1D) quantum wire. For a fixed mesh width, the error in the current conservation converges exponentially to zero with respect to the polynomial degree of the finite elements as it can be expected from theory.[22] The flexibility of the method to model geometries especially with curvilinear boundaries is demonstrated by reproducing features of the AB oscillations of the transmission through a ring structure threaded by a δ-function-type magnetic flux density.

The benefits of the method for simulating 2DEGs of almost macroscopic extent are demonstrated by computing the scattering states and their spatial electron density distributions for magnetotransmission through the specimen discussed in the thesis by Metzger.[28] Beyond the reproduction of the semiclassical magnetotransport properties, we have access to the fine structure of the transmission properties due to the wave nature of the electrons. The quantum-specific part of the magneto-transport turns out to be very sensitive to subtle changes in the details of the geometry.

The paper is organized as follows. Section II summarizes the model and the finite-element method for ballistic electron transport. Section III explains the Hardy space infinite-element technique. In Sec. IV, the method is validated against the analytically known transmission properties of the quantum wire and the Aharonov-Bohm ring. Section V shows that the Hardy space infinite-element method is capable of creating a realistic model of a magnetic focusing device of which only a small part accounts for the direct-current transport. In the concluding Sec. VI, the main results are summarized and future perspectives are indicated.

II. FEM FOR QUANTUM TRANSPORT

As a typical example for a quantum transport experiment, a general, four-terminal setup is sketched in Fig. 1. The sample region is denoted as Ω and comprises the perfect leads of infinite length and the subdomain where the scattering occurs.

Electrons can enter and leave the scattering domain only via the perfect leads, which by definition have constant widths.

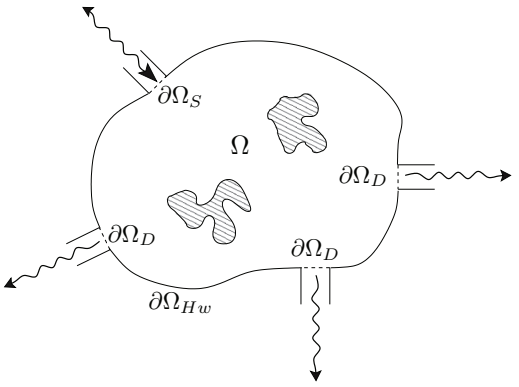

FIG. 1. Sketch of scattering experiment. The hatched areas indicate regions containing scatters. Ω: sample region; $\partial\Omega_S$: source contact; $\partial\Omega_D$: drain contacts.

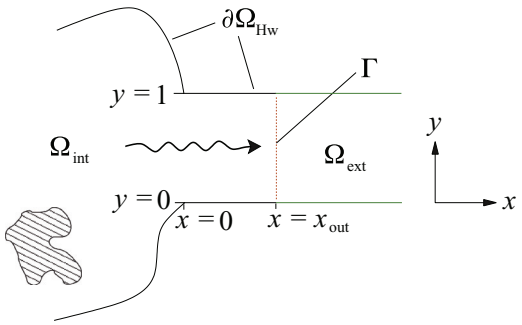

FIG. 2. (Color online) Sketch of outlet interface to exterior domain. The dotted line separates the semifinite domain Ω_{int} of the interior problem from the infinite exterior domain Ω_{ext}.

Any additional transverse potential in a lead is invariant under longitudinal translations. Sections of the lead where the potential varies in the longitudinal direction must be included in the scattering domain.

The walls of the leads and the impenetrable part of the boundary $\partial\Omega$ of the scattering domain are denoted as $\partial\Omega_{Hw}$. The contacts between the leads and the scattering domain are referred to as either $\partial\Omega_S$, for a source lead, or as $\partial\Omega_D$ for drain leads. In experiments, it is common practice to connect leads to the sample by quantum point contacts (QPCs). These are modeled as short narrow constrictions of the leads close to $\partial\Omega_D$ and $\partial\Omega_S$ (cf. Fig. 10).

In the following, we only consider geometries with two leads. One acts as source and the other as drain. In the case of the magnetic focusing simulations in Sec. V, finite sections of the hard walls will be made transparent in order to simulate a system with infinite extent in certain directions. This can be considered as a generalization of the four-terminal setup in Fig. 1.

We want to use finite elements for discretizing the Schrödinger equation. Thus, we have to design a computational domain of finite extent. To do this, we subdivide the domain Ω into a finite interior part Ω_{int} consisting of the scattering domain and the sections of the leads close to $\partial\Omega_S$ or $\partial\Omega_D$ (cf. Fig. 2) and a part Ω_{ext} containing the unbounded exterior parts of the leads. The edge interfacing Ω_{int} and Ω_{ext} at the cutoff is denoted as Γ. The finite-element computations are done on Ω_{int}, whereas the influence of the wave propagation in Ω_{ext} is put into suitable boundary conditions at Γ.

Within the leads, the coordinate x denotes the longitudinal coordinate and points away from Ω_{int}. The transverse coordinate is y. The coordinates (x,y) in the leads are local ones, i.e., $x=0$ denotes the interface to the scattering domain. We will use this convention throughout this work as the meaning of x and y is usually obvious from the context.

At zero temperature, in the absence of any interaction, electron transport can be considered as quantum mechanically coherent. In the linear limit, i.e., zero transport voltage, only the electrons at the Fermi level with energy E_F and wavelength λ_F contribute to the current.

For these electrons, the contribution of an incident mode ψ_p in the source to the wave function in a drain lead far away from the scattering domain can be written as a superposition of plane waves

$$\Psi_p = \sum_q t_{pq}\psi_q, \tag{1}$$

$$\psi_q = g_q(y)e^{ik_q x}, \tag{2}$$

where q counts the occupied states in the drain. The contributions to the individual drain modes are measured by scattering amplitudes t_{pq}. For simplicity, we assume that the states in the source and drain leads with respect to their local coordinate systems are given by the same set of orthogonal functions $\{\psi_p\}_{p\in\mathbb{N}}$.

The details of the transverse potential in the drain determine the shape of the transverse profile $g_q(y)$ of the wave function and the distribution of the energy levels

$$\varepsilon_q = E_F - k_q^2 \tag{3}$$

due to the transverse confinement. Current is carried only by those modes for which longitudinal wave numbers $k_q = \sqrt{E_F-\varepsilon_q}$ are real.

The functions $g_q(y)$ solve the transverse eigenproblem in a lead and are mutually orthogonal. Units are chosen such that the effective mass of the electron, its charge, and Planck's constant are one (see Sec. II B). Normalization of the functions g_q is chosen such that

$$\int_{\partial\Omega_X} |g_q|^2 = 1, \quad X\in\{S,D\}. \tag{4}$$

A. Quantum conductance

In a lead of finite width L, the net current density for an arbitrary wave function Ψ is given by the normal component which can be obtained by computing the contribution flowing in the direction of the outbound normal $\mathbf{n}$ of the channel cross section

$$\mathbf{j}(y) = \frac{\hbar}{m^*}\mathrm{Im}(\Psi\partial_n\Psi^*), \tag{5}$$

where $\partial_n = \mathbf{n}\cdot\nabla$ is the normal derivative and m^* is the effective mass. Integrating over the lead's cross section gives the normal component of the current

$$J = \frac{\hbar}{m^*}\mathrm{Im}\left(\int_0^L dy\,\Psi(x_{\mathrm{out}},y)\partial_n\Psi^*(x_{\mathrm{out}},y)\right), \tag{6}$$

where x_{out} is the longitudinal coordinate denoting the position where the lead is cut off (see Fig. 2).

The wave function and thus the probability current in Eq. (6) depend on the incoming mode p. Normalizing the current with respect to the current of the incoming mode of wave number $k_p = p\pi$, i.e., to divide the current by $\hbar k_p/m^*$, gives the transmission probability

$$T_p(\Psi_p) = \frac{m^*}{\hbar}J_p/k_p. \tag{7}$$

The total transmission T is given by summing over p, i.e., the contributions due to all open input modes

$$T = \sum_p T_p(\Psi_p) = \frac{m^*}{\hbar}\sum_p J_p/k_p. \tag{8}$$

The unknown amplitudes $t_{pq} \in \mathbb{C}$ are determined by the details of the scattering mechanism and the particular input mode ψ_p in the source lead. Provided both leads have the same shape and mode p is used as input, utilizing the decomposition given in Eq. (1) the conductance between the source and one drain lead is given by the well-known Landauer-Büttiker formula[10]

$$G = \frac{e_0^2}{2\pi\hbar} T = \frac{e_0^2}{2\pi\hbar} \sum_p \sum_q \frac{k_q}{k_p} |t_{pq}|^2, \tag{9}$$

where e_0 is the elementary charge.

B. Single-electron description

The wave function Ψ describing our scattering state on Ω is determined by the stationary Schrödinger equation

$$\frac{1}{2m^*}\left[\left(\frac{\hbar}{i}\nabla - q\mathbf{A}(\mathbf{x})\right)^2 + V(\mathbf{x}) - E\right]\Psi = 0 \tag{10}$$

of a single electron with effective mass m^*, charge q, and total energy E in the presence of a vector potential $\mathbf{A}(\mathbf{x})$ giving rise to a static magnetic field. In our applications, E is going to be the Fermi energy E_F. The model is completed by a suitable set of boundary conditions to describe hard walls and the semi-infiniteness of the leads.

For a constant magnetic field within the scattering domain Ω we use the Landau gauge $\mathbf{A}(\mathbf{x}) = B(-y,0,0)^T$. Throughout this work, B is considered as the primary control parameter. Depending on the spatial scale a, the dimensionless quantities $(2m^*a^2/\hbar^2)E \to E$, $(qa/\hbar)\mathbf{A} \to \mathbf{A}$, $a\nabla \to \nabla$, $(2m^*a^2/\hbar^2)qV \to V$ lead to the final dimensionless Schrödinger equation

$$[-\nabla^2 + 2i\mathbf{A}\cdot\nabla + |\mathbf{A}|^2 + V - E]\Psi = 0. \tag{11}$$

The spatial scale a (corresponding to the lattice parameter in tight-binding calculations) is assumed to be in the range 0.1 to 1 μm. As effective mass we can use the one of GaAs, i.e., $m^* = 0.067m_0$ at 0 K when measured in units of the mass of a free electron m_0.

At those parts $\partial\Omega_{Hw}$ of the boundary $\partial\Omega$ where no leads are attached to the scattering domain Ω_{int} the wave function is subject to perfectly hard walls, i.e., we have used homogeneous Dirichlet conditions

$$\Psi|_{\partial\Omega_{Hw}} = 0. \tag{12}$$

Especially for waveguides the choice of hard walls is not optimal. To achieve a more realistic description of 2DEGs in waveguides, one rather has to use a parabolic potential along the transverse coordinate of a waveguide. Some distance away from the waveguide, the parabolic potential would have to be cut off at some finite value. Therefore, an accurate model of the wave propagation transverse to the waveguide would require transparent boundary conditions along the walls as well. This poses no problem as such terms are simply incorporated into the potential energy landscape $V(\mathbf{x})$. It does not play a role for the transparent boundary conditions either, as Eq. (30) shows. The potential only enters the integral over the set of artificial cutoffs $\{\Gamma_c\}_c$. The only restriction is that $V(\mathbf{x})$ does not vary with respect to the radial direction in the truncated part of the domain.

In the leads, far away from the scattering domain the scattered part of the electron's wave function has to match the free-particle behavior, i.e., it has to fulfill Sommerfeld's radiation condition

$$\lim_{x\to\infty} x^{\frac{1}{2}}\left(\partial_x - ik\right)\Psi|_{\partial\Omega_D} = 0. \tag{13}$$

C. Variational formulation

By construction, finite elements are only applicable to bounded domains. Obviously, this contradicts leads of infinite length. The semi-infinite extent of the leads has to be modeled by surrogate boundary conditions which allow an outgoing wave to pass without any artificial reflections. Sommerfeld's radiation condition (13) essentially fulfills this, but for numerical purposes its direct application is impractical. Instead, we construct the boundary conditions from Hardy space infinite elements[23] which basically are a transformation of Sommerfeld's radiation condition to the unit circle. The zero-Dirichlet boundary conditions modeling the hard walls are directly built into the function space in which the solution is sought. The weak form is obtained from multiplying both sides of Eq. (11) with a test function Φ and integrating over $\Omega = \Omega_{\text{int}} \cup \Omega_{\text{ext}}$:

$$-\int_\Omega \Phi\nabla^2\Psi + 2i\int_\Omega \Phi\mathbf{A}\cdot\nabla\Psi + \int_\Omega \Phi[|\mathbf{A}|^2 + V - E]\Psi = 0. \tag{14}$$

For scalar products we introduce the shorthand notation

$$(u,v)_D := \int_D uv, \tag{15}$$

where D is the domain of integration and u and v are some functions defined on D. If D denotes a subset of the boundary, u and v denote the restrictions to it.

The weak form is obtained by integrating by parts which removes one derivative of the solution. To this end, we explicitly write $(\cdot,\cdot)_\Omega = (\cdot,\cdot)_{\Omega_{\text{int}}} + (\cdot,\cdot)_{\Omega_{\text{ext}}}$ and integrate on both subdomains independently. In the arising boundary terms $(\cdot,\cdot)_{\partial\Omega_{\text{int}}}$ and $(\cdot,\cdot)_{\partial\Omega_{\text{ext}}}$, we denote by $\mathbf{n}_{\text{int}}$ the outer normal of the interior domain Ω_{int} and by $\mathbf{n}_{\text{ext}}$ the outer normal of the exterior domain Ω_{ext}. At the interfaces Γ where Ω_{int} and Ω_{ext} have a common edge, both normals are opposite to each other $\mathbf{n}_{\text{int}}|_\Gamma = -\mathbf{n}_{\text{ext}}|_\Gamma$. The test functions Φ are chosen such that they vanish on $\partial\Omega_{Hw}$ so that only the boundary terms at the interfaces Γ remain. To emphasize that we are going to treat interior and exterior differently, the integrals on the exterior part will be given explicitly. Then, the weak form formally reads as

$$\begin{aligned}&(\nabla\Phi,\nabla\Psi)_{\Omega_{\text{int}}} + (\Phi,[|\mathbf{A}|^2 + V - E]\Psi)_{\Omega_{\text{int}}}\\ &+ (\Phi,2i\mathbf{A}\cdot\nabla\Psi)_{\Omega_{\text{int}}} - (\Phi,\partial_{n_{\text{int}}}\Psi)_\Gamma\\ &+ \int_0^\infty\int_\Gamma \nabla\Phi\cdot\nabla\Psi + 2i\Phi\mathbf{A}\cdot\nabla\Psi + \Phi[|\mathbf{A}|^2 + V - E]\Psi\\ &- \int_\Gamma \Phi\partial_{n_{\text{ext}}}\Psi = 0.\end{aligned} \tag{16}$$

To simplify notation, we define the bilinear forms $a(\cdot,\cdot)$ for the interior problem

$$a(\Phi,\Psi) := (\nabla\Phi,\nabla\Psi)_{\Omega_{\text{int}}} + (\Phi,[|\mathbf{A}|^2 + V - E]\Psi)_{\Omega_{\text{int}}} + (\Phi,2i\mathbf{A}\cdot\nabla\Psi)_{\Omega_{\text{int}}} \tag{17}$$

and $b(\cdot,\cdot)$ for the sum of the exterior problems in the truncated part of the leads which eventually will give us the required transparent boundary conditions

$$b(\Phi,\Psi) := \sum_c (\nabla\Phi,\nabla\Psi)_{\Gamma_c\times\mathbb{R}^+} + (\Phi,[|\mathbf{A}|^2 + V - E]\Psi)_{\Gamma_c\times\mathbb{R}^+} + (\Phi,2i\mathbf{A}\cdot\nabla\Psi)_{\Gamma_c\times\mathbb{R}^+}. \tag{18}$$

For the drain lead, the surface integrals in Eq. (16) cancel each other. In the source lead, the wave function consists of an incoming plane-wave part f and a contribution due to the backscattering at the contact. As Ψ describes the scattered part of the wave function, the surface integrals do not cancel and the surface integral over f remains. This yields the right-hand side

$$f(\Phi) := (\Phi,\partial_{n_{\text{ext}}} f)_{\Gamma_{\text{in}}}, \tag{19}$$

where Γ_{in} is the interface to the source lead. The final form of our variational problem is

find $\Psi \in X \subset H^1(\Omega_{\text{int}})$ such that $\forall\ \Phi \in X$:

$$a(\Phi,\Psi) + b(\Phi,\Psi) = f(\Phi). \tag{20}$$

The terms due to the interior problem can be treated by standard FEM. The details of how to set up the solution space X is discussed in the thesis by Nannen.[22] The space $H^1(\Omega_{\text{int}})$ consists of all functions defined on Ω_{int} which are square integrable and whose partial derivatives are square integrable as well.

All computations are based on the finite-element library *deal*.II.[29] As *deal*.II only works on meshes based on quadrilateral or hexahedral cells, all of its finite elements are implemented as tensor products of univariate polynomials. Throughout this paper, we use the standard Lagrange elements which are based on polynomials of total degree p. In two dimensions, these are defined as

$$Q_p = \left\{ u(x,y) = \sum_{0\leqslant i,j\leqslant p} a_{ij} x^i y^j \right\}. \tag{21}$$

The finite elements themselves are then given by all functions $u : \Omega \to \mathbb{R}$ of which the restriction to a cell K is an element of Q_p.[30] The power of *deal*.II lies in the fact that the rather high-level and problem-adapted description as, e.g., given in Eq. (17) suffices to reconstruct our implementation because the evaluation of the underlying integrals is provided by the library.

III. HARDY SPACE INFINITE ELEMENTS

For the exterior problem, we have to convert the integral over the longitudinal coordinate into an integral over a finite domain to make the integral exist in the sense of Lebesgue.

A. Converting $\int_0^\infty$ to $\int_0^{2\pi}$

The inapplicability of finite-element methods to infinite domains forces us to model the leads as finite stubs by truncation at x_{out} (see Fig. 2). To recover the infiniteness of the domain, we employ so-called Hardy space infinite elements as developed in the thesis by Nannen.[22] In contrast to other methods, Hardy space infinite elements are formally exact and lead to a rather sparse matrix for the discretized boundary conditions. Hardy spaces have been named in honor of Hardy's work[31] on the mean value of the modulus of an analytic function on the boundary of a circle which lays the functional analytic foundation for considering them as boundary values of functions defined only on the interior of a circle. For an overview about the theory of Hardy spaces, see the monograph by Duren.[32]

HSE map the longitudinal coordinate x of the unimportant exterior subdomain onto the unit circle so that $\int_0^\infty$ is transformed into $\int_0^{2\pi}$. This is achieved by applying a Möbius transformation $\mathcal{M}_{\kappa_0}$ to the Laplace transform $\hat{u}(s)$ of the wave function $u(x)$ with respect to the longitudinal coordinate

$$u(x) \overset{\mathcal{L}}{\longmapsto} \hat{u}(s) \overset{\mathcal{M}_{\kappa_0}}{\longmapsto} \hat{U}(z). \tag{22}$$

The Laplace transform $\mathcal{L}$ maps the real axis to another straight line through the origin in the complex plane and $\mathcal{M}_{\kappa_0}$ maps the line onto the boundary of the unit disk. If there is no ambiguity, we drop the index κ_0 of $\mathcal{M}$. Given a function $u(x) : \mathbb{R}^+ \to \mathbb{C}$ we will denote its $\mathcal{ML}$ transform as $\hat{U}(z)$. Applied to a univariate plane wave with wave number k and amplitude $u_0 \in \mathbb{C}$, this chain of transformations looks as follows:

$$u_0 e^{ikx} \overset{\mathcal{L}}{\longmapsto} \frac{u_0}{s - ik} \overset{\mathcal{M}_{\kappa_0}}{\longmapsto} \frac{-iu_0}{\kappa_0(z+1) - k(z-1)}. \tag{23}$$

This results in a finite-element formulation[23] which for the interior domain of interest keeps the usual notion of approximating the wave function as a function of position in space, whereas on those parts of the boundary representing the cutoff cross sections of the leads a different set of tensor-product polynomials is used. For the longitudinal direction, they may be thought of as modeling the behavior in a generalized frequency domain while keeping the spatial dependency for the transverse direction.

The most important tool for converting the integrals over the semi-infinite domain of the leads into integrals over some finite domain is the following identity[22] based on Cauchy's integral theorem:

$$(u,v)_{\mathbb{R}^+} = \int_0^\infty u(r)v(r)dr = \frac{1}{2\pi i}\int_{\kappa_0\mathbb{R}} \hat{u}(s)\hat{v}(s)ds = \frac{\kappa_0}{i\pi}\int_0^{2\pi} \hat{U}(e^{-i\theta})\hat{V}(e^{i\theta})d\theta = \frac{\kappa_0}{i\pi}(\hat{U},\hat{V})_{S^1}. \tag{24}$$

Mapping the tilted real axis to the unit circle S^1 is achieved by the Möbius transformation

$$\varphi(z) := i\kappa_0\frac{z+1}{z-1}, \quad z = e^{-i\theta},\ \text{Re}\kappa_0 > 0, \qquad (\mathcal{M}f)(z) := \frac{1}{z-1} f[\varphi(z)], \quad f : \kappa_0\mathbb{R} \to \mathbb{C}. \tag{25}$$

Due to the symmetry properties of the exterior domain $\Omega_{\text{ext}} = \mathbb{R}^+ \times \partial\Omega_c = \mathbb{R}^+ \times [0,1]$ we can use a separation ansatz factoring out the longitudinal direction x,

$$\Psi(x,y) = \psi(y)u(x), \tag{26}$$

$$\Phi(x,y) = \phi(y)v(x), \tag{27}$$

and apply the $\mathcal{ML}$ transform to the longitudinal direction

$$\mathcal{ML}\Psi(x,y) = \psi(y)(\mathcal{ML}u)(z), \tag{28}$$

$$\mathcal{ML}\Phi(x,y) = \phi(y)(\mathcal{ML}v)(z). \tag{29}$$

Let us first apply the HSE method to a simplified case in which there is no vector potential in the leads (independent of the issue of how to realize this in an experiment). Due to the separation ansatz and the fact that on Ω_{ext} the potential only depends on the local transverse coordinate y (cf. Fig. 2), the scalar products factorize as

$$\begin{aligned}(\nabla\Phi,\nabla\Psi)_{\Omega_{\text{ext}}} + (\Phi,[V-E]\Psi)_{\Omega_{\text{ext}}} \\ = (\phi_y,\psi_y)_\Gamma(u,v)_{\mathbb{R}^+} + (\phi,\psi)_\Gamma(u_x,v_x)_{\mathbb{R}^+} \\ + (\phi,[V-E]\psi)_\Gamma(u,v)_{\mathbb{R}^+}.\end{aligned}$$

Derivatives with respect to a coordinate are indicated by indices. By applying Eqs. (28) and (29), we get as weak formulation of the transparent boundary condition

$$\begin{aligned}\frac{i\pi}{\kappa_0} b(\Phi,\Psi) = \sum_{c\in\{\text{contacts}\}} [\{(\phi_y,\psi_y)_{\Gamma_c} + (\phi,[V-E]\psi)_{\Gamma_c}\}(\hat{U},\hat{V})_{S^1} \\ + (\phi,\psi)_{\Gamma_c}(\hat{U}_x,\hat{V}_x)_{S^1}].\end{aligned} \tag{30}$$

B. Test and ansatz functions

In order to use the standard FEM approach, we still need to define a finite-dimensional subspace of the functions on the unit circle. This is accomplished by using the span of a finite set of complex trigonometric monomials restricted to the unit circle:

$$\{z^0, z^1, \ldots, z^{n_H}\}, \quad z = e^{i\theta},\ \theta \in [0,2\pi). \tag{31}$$

For details of the arising matrices, see Refs. 23 and 24. The number n_H of degrees of freedom in the Hardy space has to be chosen such that the results, i.e., the transmission values, converge sufficiently well.

IV. TEST OF THE METHOD

To validate the HSE method, we consider a simple quantum wire and study the different aspects of the quality of the numerical solution. The capability of dealing with magnetic fields is tested on the AB effect.

A. Dependence on HSE parameters

In all our calculations, we did not find any significant effect of the HSE parameters κ_0 and n_H on the current conservation, provided the method is correctly employed, that is, κ_0 defines a line that does not intersect with the spectrum of the Hamiltonian. Especially, the simulations in Sec. V show that even in the quasiclassical limit for high energies, $n_H = \mathcal{O}(1)$ to $\mathcal{O}(10)$ suffices. Therefore, in the following we rather focus on the effects on the numerical error induced by using different finite elements and mesh widths.

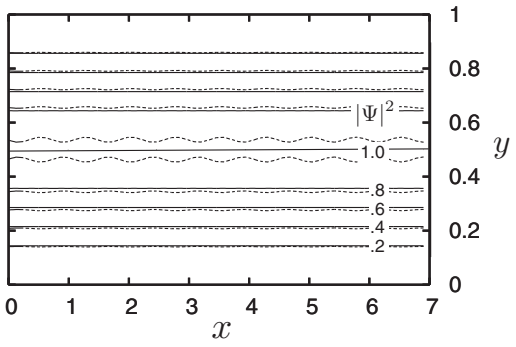

FIG. 3. Higher-order FEM solution (solid line) vs linear elements (dashed line). Contour lines represent electron density $|\Psi|^2$, $E_F = 28$, $L_x = 6.9$, $n_{\text{DoFs}} = 1026$.

B. Perfect lead

Figure 3 shows a contour plot of the electron density $|\Psi|^2$ in a perfect lead for two different polynomial degrees of the finite elements. Since the lead is empty, the analytic solution for a wave incident from the left is $\Psi(x,y) \propto \sin(\pi y)e^{ikx}$. The electron density $|\Psi|^2 \propto \sin^2(\pi y)$ is translation invariant with respect to the longitudinal coordinate x. For numerical purposes, the normalization is such that $\Psi(x,0.5) = 1$. We choose $L_x = 6.9$ as length in the x direction and $L_y = 1$ as width. For linear elements, the mesh widths are $h_x = 0.121$ and $h_y = 0.125$. For the quartic elements, $h_x = 0.484$ and $h_y = 0.5$ are used. In both cases, we have 9 degrees of freedom (DoFs) on the width of the lead and 1026 DoFs in total. As Fig. 3 shows, at this resolution the linear elements still produce some wiggling structure in the x direction whereas the quartic elements produce a constant profile. Real and imaginary parts of the wave function have the correct phase shift of $\pi/2$. It is known[26,27] that linear finite elements without further effort concerning the stabilization of the numerical solution scheme are not an optimal choice for the wave equation and that they lead to considerable phase errors in Helmholtz problems. As discussed in the recent review[27] by Thompson, it is also an accepted fact that higher-order elements are an effective remedy against unphysical dispersion artifacts in the discrete solution.

C. Perfect lead with potential barrier

The quality of the current conservation in the presence of a scatterer is studied next. Results are shown in Figs. 4 and 5. We use a simple step barrier of height $U = 20$ and length $L = 2.25$ in a section of an infinite wire with domain $\Omega_{\text{int}} = [0,x_{\text{out}}] \times [0,1]$ with $x_{\text{out}} = 6$ (see inset of Fig. 4). From the transmission T_p and reflection probability R_p of the different input modes $e^{i\sqrt{E_F-\varepsilon_1}x}\sin(p\pi y)$, $p = 1,2,3,\ldots,$ we compute the conductance from Eq. (8). Together with the corresponding error $R_0 + T_0 - 1$ of the current conservation in the contribution of the ground-state mode, we plot T as function of the Fermi energy in Fig. 4. We only show the error

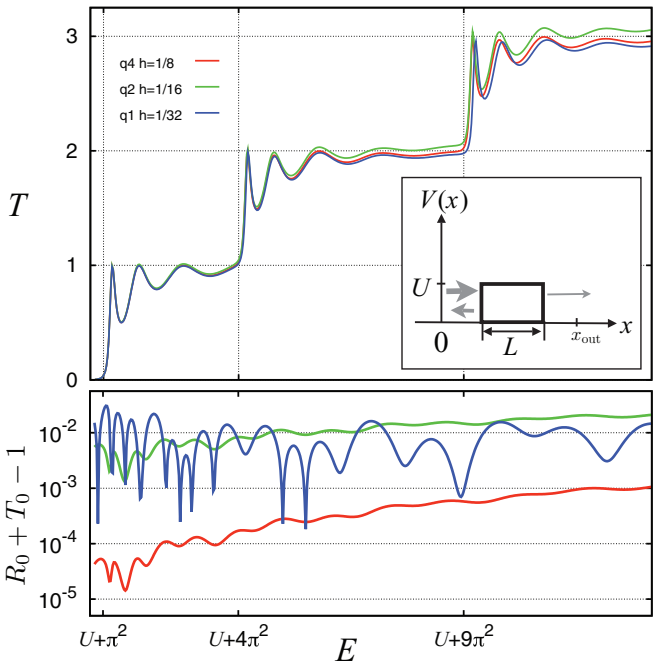

FIG. 4. (Color online) Transmission T (top) and current conservation $R_0 + T_0 - 1$ in the contribution of the ground-state mode (bottom) vs energy E for various mesh widths h and finite elements for a fixed total number of DoFs. Inset: Sketch of system.

of the ground-state mode because the total error is the sum of the individual errors and apart from a shift along the energy axis the behavior of the error with respect to the mesh width is the same for all modes. The transmission shows the expected quantization and oscillations near its jumps as it can be found in standard textbooks. The steps in the conductance reflect the number of open modes, whereas the oscillatory behavior is related to the barrier length. To compare the quality of the current conservation, three combinations of finite elements and a number of mesh refinements are used, which all lead to the same number of DoFs. The underlying coarse grid consists of six cells of size 1×1. Since for two-dimensional computations *deal*.II only provides quadrilateral cells, all finite elements are constructed from tensor products. Thus, on a cell of the mesh, an element of degree p can be represented by the polynomials of total degree p as given in Eq. (21). For linear elements (Q_1), the mesh is refined five times so that the final mesh

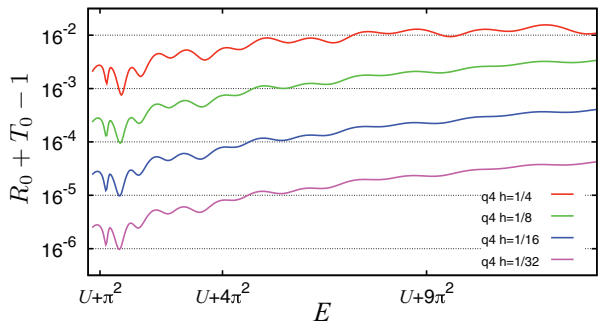

FIG. 5. (Color online) Consistent with finite-element theory, the error of the current conservation scales like h^4 for Q_4 elements [cf. Eq. (21)].

width is $h = \frac{1}{32}$. For quadratic elements (Q_2) which (away from the domain boundaries) have two degrees of freedom per coordinate direction per cell, the mesh width is $h = \frac{1}{16}$. Similarly, quartic elements (Q_4) have 4 degrees of freedom per coordinate direction per cell and require only $h = \frac{1}{8}$ to obtain the same number of DoFs. The lower part of Fig. 4 clearly shows that higher-order elements pay off by two effects. On the one hand, the error behavior for elements of even order is much smoother than for elements of odd order, especially linear ones. On the other hand, although Q_4 elements are employed on the coarsest grid, the error in the current conservation is by almost two orders of magnitude smaller than for Q_2 elements. This can be understood by looking at the trace theorems from finite-element theory[33] which predict that the error in Eq. (6) induced by replacing the exact wave function by the numerically computed one should scale like h^q where q is the polynomial order of the element. Hence, in case of Q_4 elements, a global refinement of the mesh by a factor of 2 should reduce the error by a factor of 16. This is highlighted in Fig. 5 by choosing a $\log_{16}$ scale for the abscissa.

D. Aharonov-Bohm effect

The simulation setup for the AB effect is a thin ring connected to two leads. The coarse grid prior to refinement is shown in Fig. 6. We use the AB vector potential

$$\mathbf{A}_{\mathrm{AB}}(\mathbf{x}) = \frac{B}{2\pi |\mathbf{x}|^2} \begin{pmatrix} -y \\ x \end{pmatrix}, \tag{32}$$

which produces a constant magnetic flux through the ring irrespective of the ring diameter. The magnetic field in the arms of the ring is zero.

In contrast to the other simulations presented in this paper, the measuring process is perpendicular to the direction of motion of the wave function. Waves in the ring propagate azimuthally. Thus, incident waves can not be fed into the ring parallel to the azimuthal direction. After injection, incident waves have to be scattered from the radial direction into the azimuthal direction. Similarly, measuring the flux at the outlet can not be done parallel to the direction of motion and the wave has to scatter from the azimuthal direction into the radial direction in order to deliver a detectable signal. We compare our results with the experiments by Cassé[34] and Hansen.[35] Both show that for rings with arms of finite width one may encounter period doubling and phase shifts in the AB oscillations, depending on the value of the Fermi energy. The coarse mesh of our model ring is shown in Fig. 6. It has an

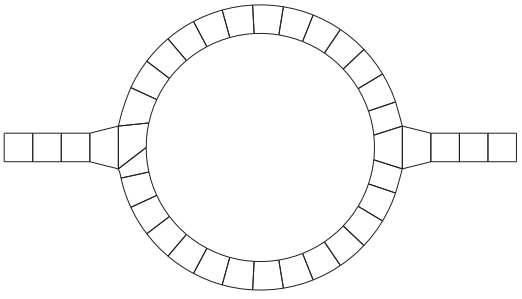

FIG. 6. Coarse grid for the Aharonov-Bohm simulation.

inner radius $R_i = 4$ and an outer one $R_o = 5$. These values are chosen such that the geometry of the scattering domain in the simulation resembles the one in Hansen's experiment[35] (cf. the inset of its Fig. 1). To roughly reproduce the experimental setup, we widen the cells forming the contacts with the ring so that the leads locally get a funnel-like shape. For high energies where several modes are active and the total transmission is given by the sum in Eq. (8), the oscillation frequency and phase may drastically change with energy as it selects which modes have a dominant contribution.[36] In the case of the AB oscillations, we are rather interested in a proof of concept and therefore use as Fermi energy $E_F = 10$ to bring out the quantum effects. Because of the way the coarse mesh is generated, the cells close to the contacts may be asymmetric, but after mesh refinement to the working resolution there are always enough DoFs to fully resolve the wave nature of the solution. We refine the mesh four times and use Q_2 elements so that there are 32 DoFs on the cross section of the contacting leads and of the arms of the ring. The comparison with an analytic solution of an infinitely thin ring requires that only one mode is active in the lead. To improve the realism of the boundary approximation, we use the isoparametric version of the Q_2 elements, i.e., both the wave function and the boundary of the ring are approximated by quadratic polynomials. We note in passing that the issue of a piecewise linear boundary should be compared with Kokoreva *et al.*[37] as corners might by interpreted as pointlike scatterers. As Hardy space parameters we use $\kappa_0 = 0.13\exp(0.2i\pi)$ and $n_H = 10$. The reason for this particular value of κ_0 is that if we chose $\kappa_0 = \sqrt{E - \pi^2}$ and $n_H = 0$, the Hardy space elements would turn into the first-order TBC

$$\partial_n \Psi = ik\Psi, \tag{33}$$

which are exact for the monochromatic case if the wave number k equals the wave number in the direction of motion, i.e., $k = \sqrt{E_F - \pi^2}$. As incident wave from the left we use the same plane wave as in Sec. IV B. The solid line in Fig. 7 is a manual fit to the AB oscillations for $E_F = 10.0$ as function of magnetic flux as predicted for a ring with one-dimensional

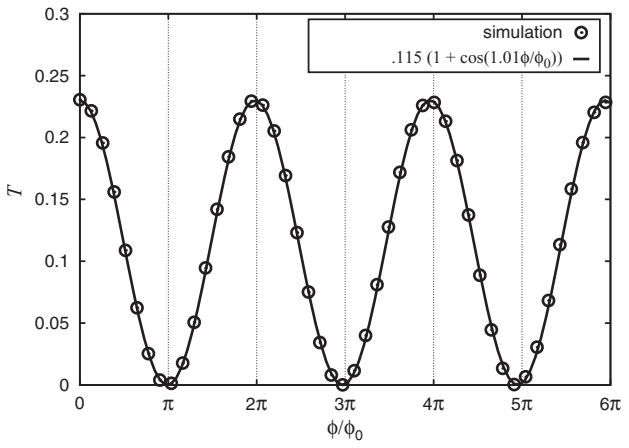

FIG. 7. Comparison of simulation results (circles) using quadratic finite elements for a fixed mesh width $h = \frac{1}{32}$ and theoretical (line) transmission T vs magnetic flux for the system shown in Fig. 6. The line is obtained from fitting the expression given in the legend.

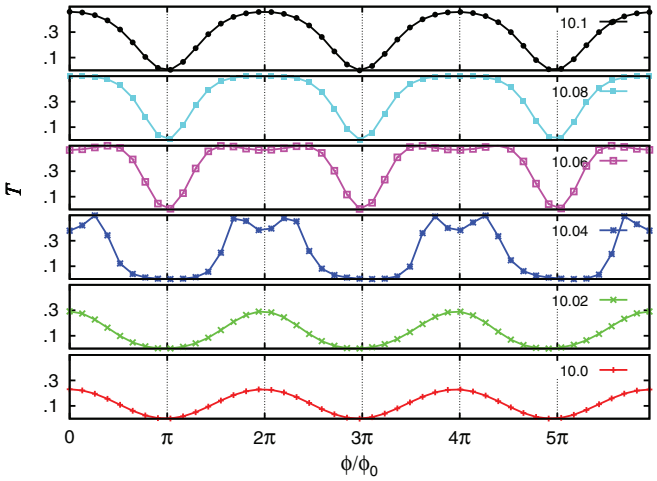

FIG. 8. (Color online) Transmission T for various energies (value given in the legend) vs magnetic flux for the system in Fig. 6 and quadratic finite elements for a fixed mesh width $h = \frac{1}{32}$.

arms

$$a_0[1 + \cos(\nu\phi/\phi_0)] \tag{34}$$

and just serve to guide the eye. As fitting parameters we use $a_0 = 0.115$ and $\nu = 1.01$. In a perfect, one-dimensional ring, the frequency should be $\nu = 1$. Figure 8 shows that similar to Fig. 4 in Hansen's paper[35] our transmission curves are very sensitive to changes in the Fermi energy. Changes of about 1% decide whether the effect of frequency doubling appears, which is comparable to experimental findings. These tests show that we are able to correctly reproduce the purely quantum mechanical effect of Aharonov-Bohm oscillations. A detailed study of the dependence on the shape of the contacts of the transmission properties of an AB ring of finite width is a project of its own which is beyond the scope this paper.

V. MAGNETIC FOCUSSING IN 2DEGS

To show the usefulness of the method for simulating quantum transport, we use the magnetic focusing device previously studied by Metzger[28] as a nontrivial benchmark. He computed the conductance from an ensemble of classical single-electron trajectories by counting how many of them reach the drain at a given magnetic field. At sufficiently high energies, the magnetoconductance computed from the classical simulation should coincide with the quantum mechanical results. Hence, one has to take into account a, possibly large, number of plane waves. Moreover, because of the size of the 2DEG device, we restrict the computational domain to the lower left corner where the actual scattering occurs. Truncation of the noninteresting part of the sample introduces additional, extended transparent boundaries. This is considerably different from the previous examples of the quantum wire and the AB device where only the leads had to be cut off at some finite length. Electrons considered as classical particles of velocity $\mathbf{v}$ in a (constant) magnetic field $\mathbf{B}$ are subject to the Lorentz force $\mathbf{F}_L = -e_0(\mathbf{v} \times \mathbf{B})$. When entering the device from the source, they move on trajectories forming circular arcs (cf. Fig. 9). From the balance of centripetal and Lorentz force follows the

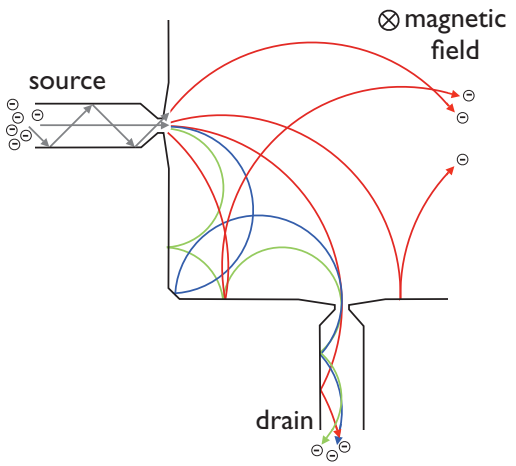

FIG. 9. (Color online) Classical electron trajectories in a previously studied (Ref. 28) magnetic focusing device. Colors indicate different strengths of the magnetic field.

classical cyclotron radius

$$R_c = \frac{m|\mathbf{v}|}{|e_0\mathbf{B}|}. \tag{35}$$

In the absence of a potential electrons of energy $E = m\mathbf{v}^2/2$ hit the drain for the first time if $R_c = R$ (cf. Fig. 10), i.e., the magnetic field strength has to be

$$B_0 = \frac{\sqrt{E}}{R}. \tag{36}$$

For higher magnetic fields, transmission occurs whenever $R_c = R/N, N \in \{1,2,\ldots\}$. Due to the fact that electrons can leave the source under different angles, there is a multitude of classical trajectories which leads to a broadening of the peaks similar to the one observed in a quantum mechanical description and to the appearance of peaks at noninteger values of N.

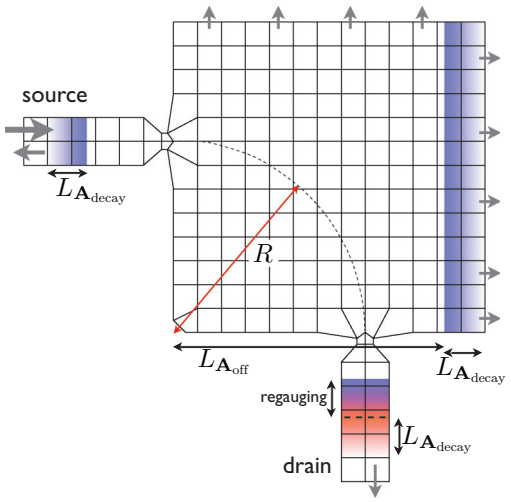

FIG. 10. (Color online) Coarse grid of the focusing device. Gray arrows indicate inbound and outbound waves on the transparent boundaries. Color gradients denote the areas where the vector potential is turned off. In the drain this must be preceded by a regauging step.

A. Details of simulation

Due to the size of the device, we only consider its physically relevant part, i.e., the lower left corner of 4×4 μm. This introduces two additional transparent boundaries in the north and east of the domain, indicated by gray arrows in Fig. 10. To directly compute the wave function, several technical issues still have to be addressed.

1. Vector potential at transparent boundaries

At boundaries parallel to the vector field (cutoff of source lead and eastern boundary), we turn off the vector potential smoothly in a strip of width $L_{\mathbf{A}_{\text{decay}}}$ (color gradient from blue to white in Fig. 10) such that no artificial reflections occur. Using the regauging method by Baranger *et al.*,[38] we can locally change the direction of the vector potential to align it with the drain lead (color gradient from blue to red in Fig. 10). After reorientation, we can proceed as in the source lead. This does not alter the quantum mechanic flux through the leads' cutoff boundaries where we measure and we may use the TBC developed in Sec. III A for the Helmholtz case.

2. Model geometry for the contacts

Much of the experimental effort is spent on connecting the leads by quantum point contacts (QPC) so that electrons entering the device from the exterior reservoirs have a well-defined electronic state and a very narrow distribution of their direction of motion. The QPCs are modeled by narrowing the leads to a third of their width where they are attached to the bulk. To model the pointlike contacts between the 2DEG and the wires, the boundary is shaped like a shallow funnel on the side of the 2DEG.

3. Choice of Fermi energy

The electron density n_{e^-} in the devices studied by Metzger[28] are 2.2 to 2.5×10^{11} cm^{-2}. From n_{e^-} we can compute the Fermi wavelength λ_F and estimate the required spatial resolution of the computational mesh. In 2D, one state in k space occupies a volume of $4\pi^2/L^2$ where L^2 is the area covered by the 2DEG. The volume of the Fermi sphere in 2D is πk_F^2. Including spin degeneracy, the number of states in the Fermi sphere is $N_{k_F} = 2\pi k_F^2/(4\pi^2/L^2)$. Dividing by the sample size gives the density $n_{e^-} = N_{k_F}/L^2 = 2\pi/\lambda_F^2$. From this we get $\lambda_F = \sqrt{2\pi/n_{e^-}}$. In the experiments discussed by Metzger, the distance R from the lower left corner to the centers of the QPCs is 3 μm. For $n_{e^-} = 2.2 \times 10^{11}$ cm^{-2}, this corresponds to 56 λ_F and 60 λ_F for $n_{e^-} = 2.5 \times 10^{11}$ cm^{-2}. For $R = 6.5a$, a the length scale from Sec. II, 1 cm corresponds to $10^4 R/3$. Thus, in our units (up to $\pm10\%$) $E_F = k_F^2 = 2\pi n_{e^-}(3 \times 10^{-4}/R)^2 \approx 3000$ and $\lambda_F = 2\pi/\sqrt{E_F} \approx 0.12a$ or 4 wavelengths per coarse grid cell.

4. Beam collimation

Additionally, we add a "door sill" potential V_{ds} in the constrictions to let only pass electrons with kinetic energy in the direction of the lead (long straight arrow in the source lead in Fig. 9). In the local coordinates of the leads, its shape is $V_{ds} = \alpha E_F \cos^2(\pi x/2L_{ds})$, $\alpha \in [0,1)$, and L_{ds} measures the

width of the door sill. Typical choices are $\alpha \in [0.85, 0.95]$ and $L_{ds} = 0.25a$. For $|x| > L_{ds}$ we set $V_{ds} \equiv 0$. Electrons with a finite amount of kinetic energy for a movement transverse to the direction of a lead (zigzagging arrows in Fig. 9) are reflected.

5. *Choice of Hardy parameters*

Before we can simulate the quantum mechanical properties of the device by solving the Schrödinger equation (11), to get the scattering states Ψ_p for the various input modes we have to check whether physical results depend on the parameters of the Hardy space transparent boundary conditions. As shown elsewhere,[39] the physical results do not particularly depend on the choice of the Hardy space parameters. Even for Fermi energies $E_F = \mathcal{O}(10^3)$ a value of $|\kappa_0| \approx 6$ and $n_H \approx 10$ gave good results, although theory[22] would suggest to choose $|\kappa_0| \approx k_F$. The coarse grid including the modifications to the vector potential is shown in Fig. 10. For all simulations shown here we use $|\kappa_0| = 5.5623$, $-i \ln \kappa_0 = 0.2\pi$, $n_H = 11$, total system size $L = R + 2.5$, $L_{\mathbf{A}_{\text{decay}}} = 0.75$, $L_{\mathbf{A}_{\text{off}}} = L - L_{\mathbf{A}_{\text{decay}}}$, and Q_2 Lagrange elements. The origin is in the lower left corner of the geometry. The source lead is parallel to the x axis and the drain parallel to the $-y$ axis. In the source lead, the decay of the vector potential starts at $x = 0$ and in the drain at $y = -0.75$. The regauging zone in the drain starts at $y = 0$. The leads always have a width $L = 1$.

6. *Simulated systems*

We use two different system sizes and Fermi energies. The small device with $R = 4.5$ and $E_F = 557.6$ (corresponding to $n_{e^-} = 2 \times 10^{10}$ cm^{-2}) serves to estimate the effect of the door sill potentials in the QPCs. To do this, we plot the electron density distribution for various characteristic peaks in the magnetoconductance (cf. Figs. 11 and 12). Especially, without door sill potentials (Fig. 11) a proper treatment of the open boundaries is crucial as many modes have to be let through at once. The large system with $R = 6.5$, $E_F = 1090.6$ ($n_{e^-} = 8.14 \times 10^{10}$ cm^{-2}), and door sill potentials of height $0.9E_F$ shows that our simulation can be close to experiments. For $E_F = 557.6$ the coarse mesh is refined four times and for $E_F = 1090.6$ five times. This yields meshes sufficiently fine to reliably compute the magnetoconductance up to the fourth peak, i.e., for classical trajectories with $R_c = R/4$. A variation in the length of the leads does not influence the transmission properties.

B. Electron densities and conductance

The classical behavior can be inferred from the wave functions Ψ_p computed independently for the different input modes. Since there is no interaction between the electrons, the total electron density is given by $\varrho(x,y) := \sum_p |\Psi_p|^2$. For improved visualization we rather work with $\sqrt{\varrho}$ and choose the plot range such that the electron flow in the bulk and in the drain is well resolved.

When plotting $\sqrt{\varrho(x,y)}$ as in Figs. 11–13, the classical trajectories should be recoverable from the ridges formed by the local maximums. In areas without self-interference, these ridges should be tangential and in areas of strong self-interference orthogonal to the trajectories. This is particularly evident for high magnetic fields which provide a sufficiently strong focusing.

The transmission probabilities are computed by applying Eqs. (7) and (8) to the cross section of the drain lead where it is cut off. The flux through the transparent boundaries in the north and east of the domain could be measured in the same way which would allow us to control the current conservation. Since this has been done already extensively on the simpler examples, this is ignored in the following.

Figures 11 and 12 show probability densities and magneto-transmission spectra for the small system with Fermi energy $E_F = 557.6$ and two different contacts to the leads. In Fig. 11, the contacts are just given by the narrowing of the leads, whereas in Fig. 12 a door sill potential has been added to further select which modes from the leads contribute to the transmission. The comparison of Figs. 12 and 13 highlights the effects of shortening the Fermi wavelength by approximately doubling the Fermi energy while the contacts remain the same.

Similar to the classical trajectories only for selected values of the magnetic field strength B, the wave function is able to penetrate from the bulk into the drain. Rescaling B with $1/B_0$ removes the dependence on the system size and reveals the universal behavior of the conductance as a function of B/B_0 [Figs. 11(e), 12(e), 14, and 15]. These figures are obtained by calculating the current [Eq. (6)] through the terminal cross section of the drain for each input mode and plotting the modal and total transmission [Eqs. (7) and (8)] against B/B_0. The dominant peaks correspond to the classical cyclotron trajectories and are mostly close to integer values of B/B_0. The fine structure present in the transmission spectra is due to the wave nature of the electrons. One observes that the current is mainly carried by modes 1 and 3 as they are the only ones which fit through the constriction. Without door sill potentials, there is also a contribution by modes 2 and 4 to the total transmission but their influence can almost be completely eliminated by the door sill potentials as Figs. 12(e) and 15 reveal. The comparison of Figs. 11(e) and 14 in Sec. V B2 gives an account of the influence of the chamfered corner.

1. *General observations*

There are several general observations which apply to all of the electron density plots:

(i) There is always a strong reflection of the input modes at the source contact. This is consistent with the ballistic electron model which implies that scattering only occurs in contacts to the leads and at hard walls.

(ii) The dispersion of the wave function shifts the peaks to values of B/B_0 lower than those expected classically.

(iii) At the artificially introduced boundaries, which are not present in the real system but which are needed to restrict the computational domain to the subregion of physical importance, spurious reflections are avoided. This is revealed in particular in the snapshots of the electron density for low magnetic fields at the eastern boundary and in general in the drain. Furthermore, the transmission curves agree well with those obtained from semiclassical simulations.[28] This would

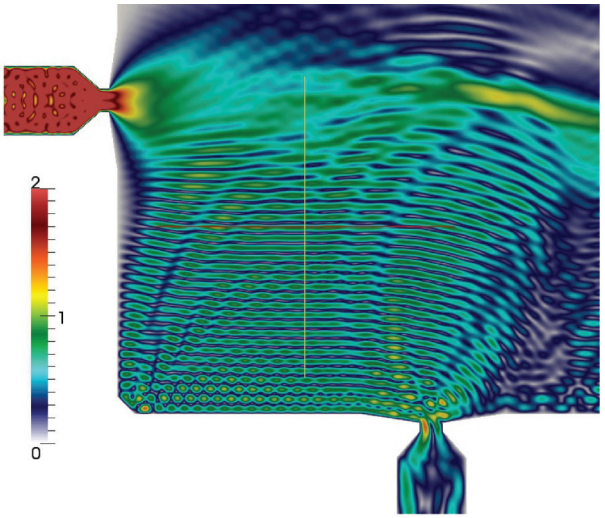

(a) $B/B_0 = 1.35$

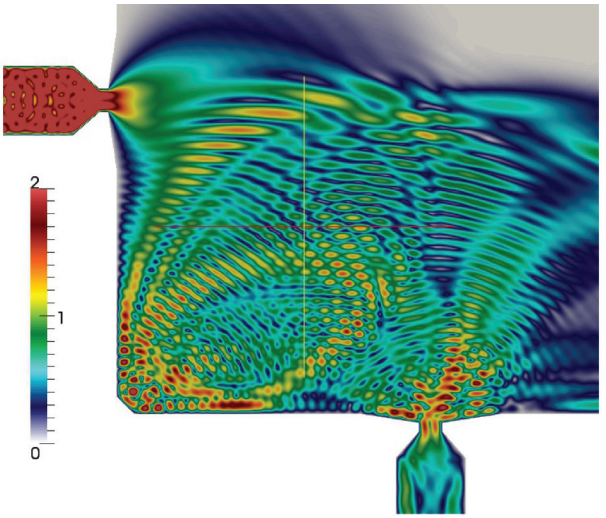

(b) $B/B_0 = 1.825$

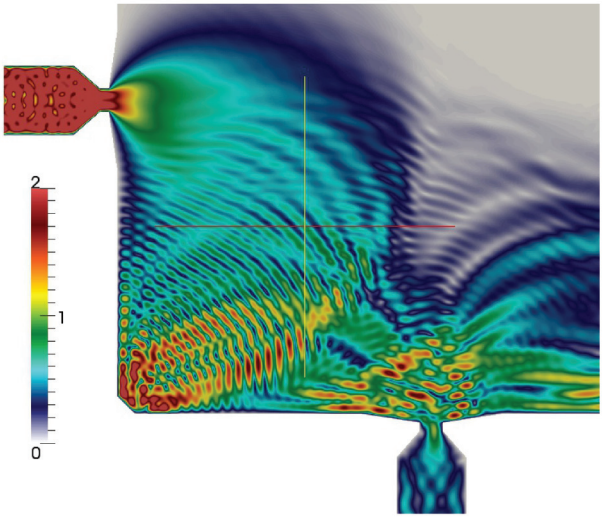

(c) $B/B_0 = 2$

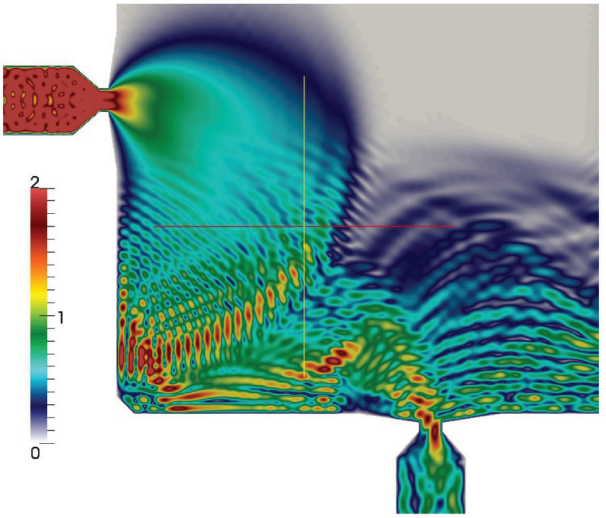

(d) $B/B_0 = 2.35$

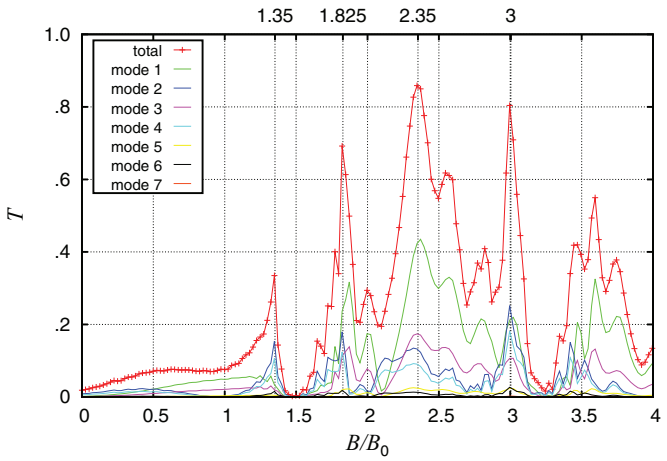

(e)

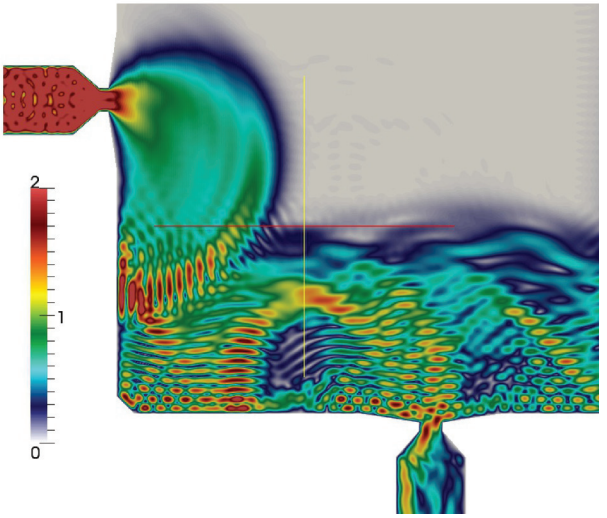

(f) $B/B_0 = 3$

FIG. 11. (Color online) Modulus of the wave function Ψ at $E_F = 557.6$ and $R = 4.5$. Distribution for the caustic peak at $B/B_0 = 1.35$ (a), split second classical peak at $B/B_0 = 1.825$ (b) and $B/B_0 = 2$ (c), broad peak at $B/B_0 = 2.35$ (d), and third classical peak at $B/B_0 = 3$ (f). The total transmission and the contribution of the individual input modes are shown in (e).

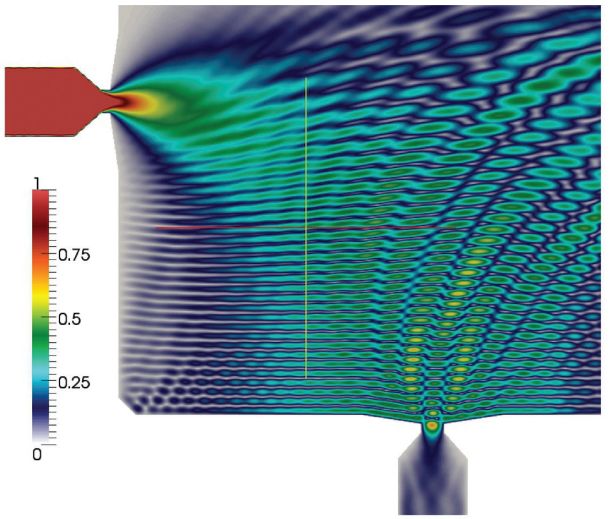

(a) $B/B_0 = 1$

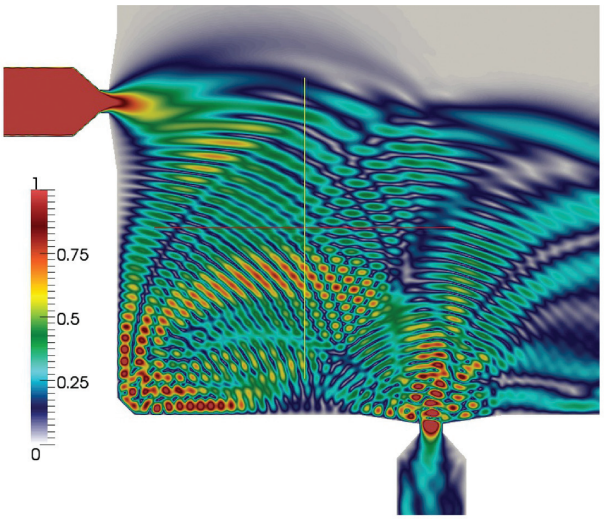

(b) $B/B_0 = 1.825$

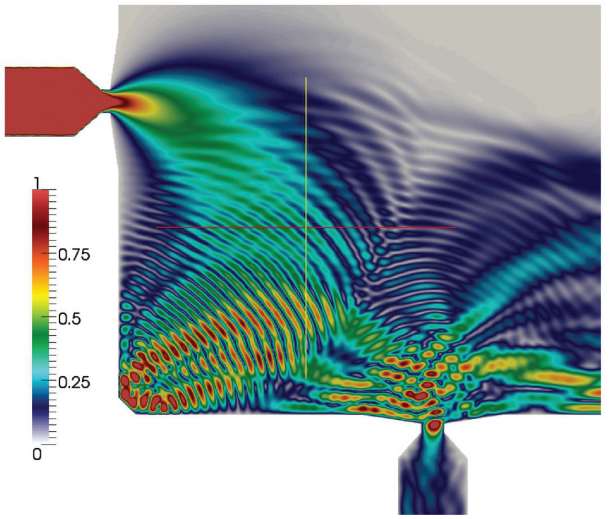

(c) $B/B_0 = 2$

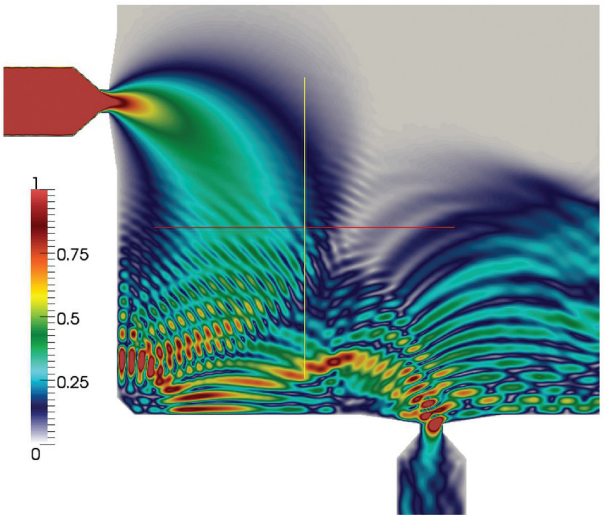

(d) $B/B_0 = 2.35$

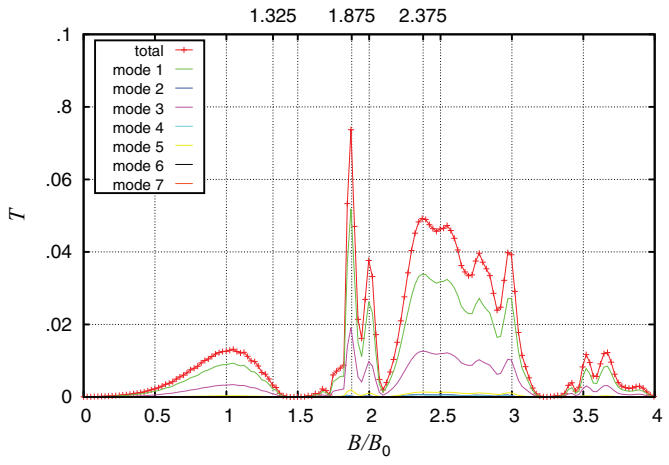

(e)

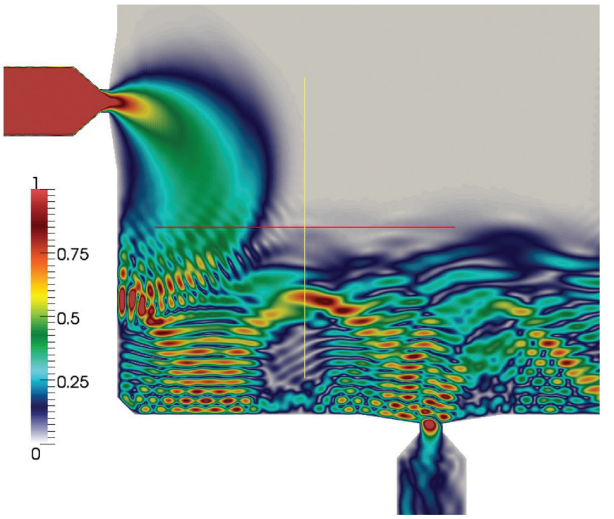

(f) $B/B_0 = 3$

FIG. 12. (Color online) Modulus of the wave function Ψ at $E_F = 557.6$, $R = 4.5$, and door sill potentials with height $0.9E_F$. Subfigures are as in Fig. 11 except for (a) which now shows the distribution for the first broad focusing peak. The strong beam collimation eliminates the caustic peak and enhances the classical peak at $B/B_0 = 2$.

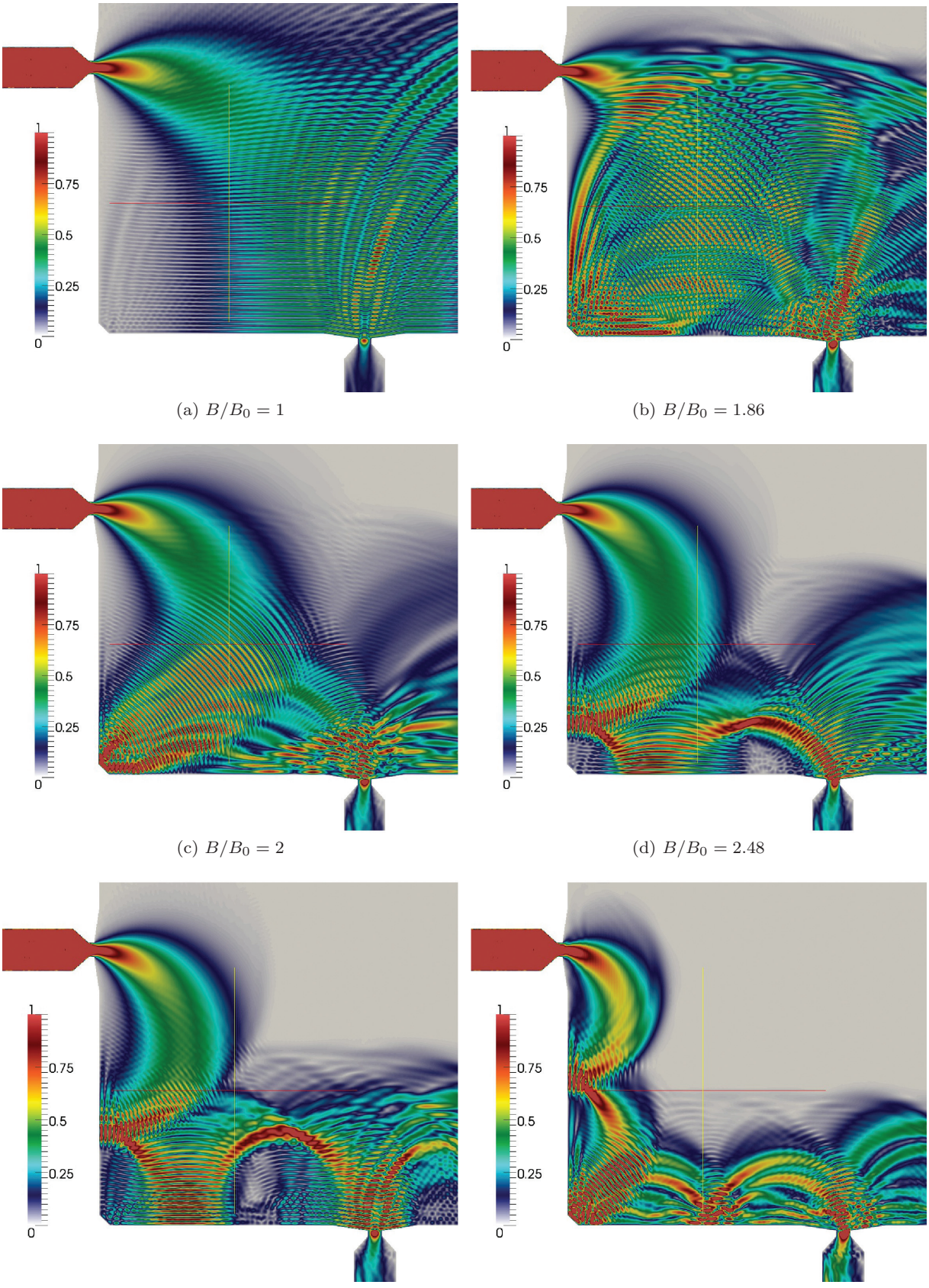

(a) $B/B_0 = 1$ (b) $B/B_0 = 1.86$

(c) $B/B_0 = 2$ (d) $B/B_0 = 2.48$

(e) $B/B_0 = 3$ (f) $B/B_0 = 3.96$

FIG. 13. (Color online) Modulus of the wave function Ψ at $E_F = 1090.6$, $R = 6.5$, and door sill potentials with height $0.9E_F$. As in Fig. 11, selected electron distributions and the total transmission and the contribution of the individual input modes are shown. Due to the shorter Fermi wavelength, it is much easier to identify the classical trajectories.

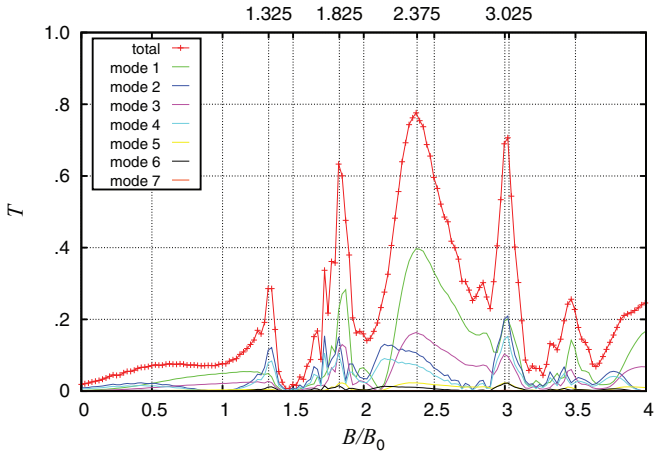

FIG. 14. (Color online) Total transmission and contribution of the individual input modes for the system shown in Fig. 11 but without chamfered corner. Peaks related to classical trajectories, e.g., at $B/B_0 = 2$, which require reflection in the corner are suppressed.

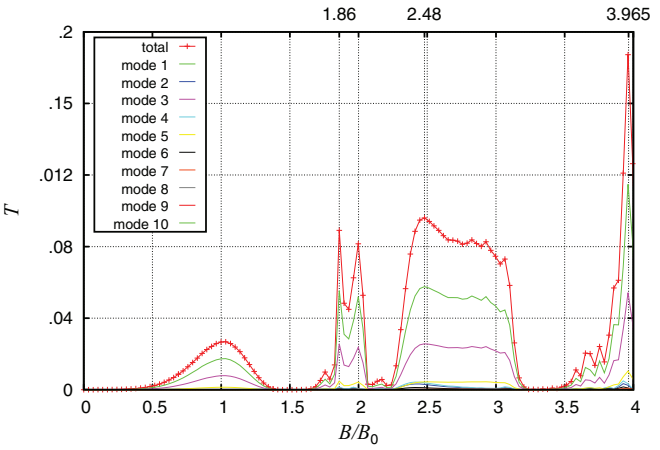

FIG. 15. (Color online) Total transmission and contribution of the individual input modes for the system with $E_F = 1090.6$, $R = 6.5$, and chamfered corner and door sill potentials with height $0.9E_F$. The strong beam collimation eliminates almost all but the classical peaks.

not be the case if the boundary conditions were not able to correctly handle the multimodal case.

(iv) Even-numbered peaks (near $B/B_0 = 2$ and 4) are subject to higher-order caustic effects. Several "trajectories" leave the corner in different directions yet they are recollimated approximately at the same location at the wall or in the contact to the drain. For the collimated beam emanating from the source, the corner breaks the focusing and splits the beam [cf. Figs. 12(c), 13(c), and 13(f)].

(v) Similar to Hall systems in the presence of a magnetic field, the current flows mostly near the boundary in the drain. Good examples for this are Figs. 11(f) and 13(f).

(vi) Similar to experiments,[13,14] we observe branched electron flow although there is no weak disorder potential in our model. In our case, the source of the branching is not the scattering of the wave function at the ripples of the weak disorder potential but rather at the various features of the shape of the geometry. The branching is especially visible in the drain where the vector potential still can focus the wave function. If the lead was infinitely wide, the QPC would be a pointlike source giving rise to a spherical wave. Yet, the funnellike shape refocuses the transmitted wave in the outlet, and the combination of reflections at the lateral walls of the lead and the magnetic field induce several ridges in the electron density similar to what is observed when the electron wave in an extended system gets scattered at the ripples of the weak disorder potential. Branching is also induced by scattering at the chamfered corner and backscattering into the bulk at the entrance to the drain lead. In this sense, the chamfered corner and the drain contact can be considered as scattering centers. In the corner device discussed here, the branching is clearly caused by interference effects.

Figure 11 shows the electron densities associated with the peaks at $B/B_0 = 1.35$, 1.825, 2, 2.35, and 3. The absence of the door sill potentials in the contacts allows the even modes to contribute to the total transmission and as a result the peak expected at $B/B_0 = 1$ turns into a shoulder of the so-called "caustic" peak at $B/B_0 = 1.35$. Classically, the caustic peak corresponds to semicircular trajectories, the diameter of which equals the distance between source and drain. The values of B in Figs. 11(b)–11(d) and 11(f) are chosen such that we can compare the quantum simulation with the classical trajectories sketched in Fig. 9. Figure 11(d) is equivalent to a trajectory leaving the source at an acute angle with the lead axis and getting reflected twice before hitting the drain.

2. *Influence of the chamfered corner*

To assess the influence of the chamfered corner, compare Figs. 11(e) and 14. In its presence, the wiggles in the T_p curves between the main peaks are more pronounced. The wiggles can be explained by self-interference effects of the spherical wave emanating from the source with its reflections at the hard walls. From the classical trajectories, one would expect that only peaks belonging to even multiples of B/B_0 would be affected which is consistent with the first peak around $B/B_0 \approx 1$ not being influenced. Yet, the shape of the curve at $B/B_0 \approx 2.4$ shows that the details of the corner can have a significant impact on the transmission. The chamfered corner enhances the contributions of the odd modes (1,3,5,7) near $B/B_0 \approx 2$ and partly eliminates the double-peak structure in the contribution of the even modes (2,4) in the vicinity of $B/B_0 \approx 1.7$.

A purely quantum mechanical feature of the T curves are the small wiggles between the main peaks. The wiggles are caused by the small local maximums in the electron density close to the hard walls which get pushed into the drain one after another when B is increased. Another interesting feature is observed when analyzing the contributions of the different modes. Consider the first structure for B/B_0 between 0.5 and about 1.5. In analogy to geometric optics, the peak at $B/B_0 \approx 1.35$ has been interpreted as a caustic peak on the basis of the trajectory sampling by Metzger.[28] The quantum mechanical treatment in this paper provides an interpretation in the sense of wave optics. From the data shown in Figs. 11(e) and 14, one notes that the contributions of the odd modes (1,3,5,7) have broad maxima at $B/B_0 \approx 1$, while the even modes (2,4,6)

contribute a split peak with a broad maximum at $B/B_0 \approx 0.5$ and a sharp peak near $B/B_0 \approx 1.35$. This is due to the fact that in the middle of the drain contact the densities of the odd modes are maximal which is not the case for the even modes. Therefore, odd modes produce a collimated beam propagating in the direction of the lead, whereas even modes produce a split beam with its two parts leaving the source under a finite angle with the lead axis. As a result of this beam splitting, one part moves on a more direct way and hits the drain already for much smaller values of B/B_0. The superposition of all of the modes smears out the already broad peak at $B/B_0 = 1$ and turns it into a shoulderlike structure of the sharp caustic peak at $B/B_0 \approx 1.35$.

3. *Electron beam collimation in the contacts*

Adding local barrier potentials in the QPCs collimates the electron beam and suppresses the caustic peak located near $1.35B_0$ and other peaks. By varying the height of the door sill potentials, it can be figured out which peaks are mostly due to electrons leaving the source under a finite angle with respect to the lead axis.

Figure 12 shows the electron densities associated with the peaks at $B/B_0 = 1$, 1.825, 2, 2.35, and 3 when a door sill potential of height $0.9E_F$ is present and eliminates the even modes. The first observation is that the total transmission is substantially reduced. Since the caustic peak is removed from the total transmission, we instead show the electron density of the first focusing peak at $B/B_0 = 1$ in Fig. 12(a). Its rather large half-width of approximately $\Delta(B/B_0) = 0.5$ can be explained by the broad charge distribution of the electron density in front of the drain contact. Without door sill potentials, the first focusing peak could only be noticed by looking at the contributions of the individual modes in Fig. 11(e). The suppression of the caustic peak agrees with the results from semiclassical methods[28] and was studied in more detail elsewhere.[39]

Figure 13 shows the electron densities associated with the peaks at $B/B_0 = 1$, 1.86, 2, 2.48, 3, and 3.96 in Fig. 15 for the system with $E_F = 1090.6$, $R = 6.5$, and with door sill potentials of height $0.9E_F$. Compared to Fig. 12, the electron densities are even closer to the classical regime due to the shorter wavelength.

As in the case of the smaller system for barrier heights close to E_F, the current is carried by the first and third modes which can be seen in Fig. 15. Almost all "nonclassical" peaks are gone due to the beam collimation. The double peak at $B/B_0 \approx 2$ is a characteristic feature of the chamfered corner.

VI. CONCLUSION

We have successfully applied the Hardy space infinite-element method to the problem of calculating the single-electron scattering wave function in quantum wires, Aharonov-Bohm rings, and in semiopen, two-dimensional electron systems. The Hardy space method is a recent development and is a novel form of transparent boundary conditions for finite-element computations in acoustic scattering.[24] This type of boundary condition allows us to truncate uninteresting parts of extended systems. Thus, we can do a full quantum mechanical calculation of the stationary scattering states in complex geometries at comparatively low computational costs.

It is possible to pair the transparent boundary conditions presented in this work with methods for solving the time-dependent Schrödinger equation.[39] This would allow us to simulate chemical reaction probabilities[40] or the transmission properties of dielectric media.[41]

With direct access to the wave function, the scattering matrix can be obtained as a function of the magnetic field, and the zero-temperature direct-current conductivity can be computed using the Landauer-Büttiker relation between quantum transmission and conductance. This provides a complete description of the quantum mechanical features of ballistic transport in a device including the local electron density. Hence, we can compare our simulation not only to conductance measurements but also to the experimentally imaged electron flows. Although not done here, given the wave function it is straightforward to compute the current density within the device.

Since the charged tip of a scanning probe microscope can be modeled as an additional term in the background potential,[16] it is also possible to simulate the experiments[12,13] and similar ones. The additional output of such simulations would be the local electron density and the local current density.

The benchmark tests for the quantum wire show that using higher-order finite elements drastically improves the quality of the numerical current conservation because of the improved phase accuracy of the numerical solution.

The Aharonov-Bohm test case demonstrates that the method is able to reproduce purely quantum mechanical interference patterns for which an accurate reproduction of the phase of the electron's wave function is crucial. In particular, we are able to work on geometries with smooth boundaries which are a much more realistic representation of the experimental setup than computational domains with piecewise linear boundaries.

The nontrivial example of the scattering states in a 2D corner device shows that, despite its complexity, the Hardy space infinite-element technique is worth the effort to implement it. It is possible to compute the wave functions for energies up to values representative for the classical limit and for electron densities typically used in experiments. Furthermore, we have studied the influence of the details of the contacts and of the shape of the sample on the transmission properties in a mode-resolved manner. We can directly establish the relationship between the individual modes and which features in the magnetoconductance curves they cause.

Considering the discussion of the problem of numerical dispersion errors in the mathematical literature, e.g., Refs. 26 and 27, it is certainly worthwhile to assess the approximation properties of different combinations of variational formulations, finite-element spaces, and rules for numerical quadrature. Especially for simulating Aharonov-Bohm–type effects, an accurate approximation of the phase information is crucial. Since increasing the strength of the magnetic field confines the wave propagation to smaller portions of the computational domain, we should also look into local mesh adaption.

Beyond these technical topics, a systematic study of various geometric effects due to the details of the shape of the boundary and the contacts should give further insight into the nature of the wave functions in the corner device when subject to a magnetic field. In a similar way, we may investigate the magnetoconductance and the electron distribution in the presence of a tunneling tip or the weak disorder potential due to the donor layer beneath the two-dimensional electron gas by a suitable choice of the potential in the Schrödinger equation. Especially, we are able to study quantitatively the crossover from the quantum mechanical to the classical behavior of electrons by varying the Fermi energy.

ACKNOWLEDGMENTS

I thank G. Lube for introducing me to the theory and practice of finite elements and for his continuous and long-standing, encouraging support. I enjoyed many fruitful discussions with T. Hohage and L. Nannen about the details of Hardy space elements. I am deeply indebted to O. Bendix, J. Metzger, and R. Fleischmann from the Max-Planck Institute of Dynamics and Self-Organization, Göttingen, for hinting me at the problem and many helpful and enlightening discussions. Finally, I also would like to thank R. Kree for carefully reading the manuscript and for many constructive discussions about the nature of quantum transport.

[1] R. Landauer, IBM J. Res. Dev. **1**, 223 (1957).
[2] M. Büttiker, Phys. Rev. B **40**, 3409 (1989).
[3] A. Aronov and Y. V. Sharvin, Rev. Mod. Phys. **59**, 755 (1987).
[4] D. Yu. Sharvin and Yu. V. Sharvin, Pis'ma Zh. Eksp. Teor. Fiz. **34**, 285 (1981) [JETP Lett. **34**, 272 (1981)].
[5] K. Klitzing, Phys. Rev. Lett. **45**, 494 (1980).
[6] B. J. van Wees, H. van Houten, C. W. J. Beenakker, J. G. Williamson, L. P. Kouwenhoven, D. van der Marel, and C. T. Foxon, Phys. Rev. Lett. **60**, 848 (1988).
[7] D. A. Wharam, T. J. Thornton, R. Newbury, M. Pepper, H. Ahmed, J. E. F. Frost, D. G. Hasko, D. C. Peacock, D. A. Ritchie, and G. A. C. Jones, J. Phys. C: Solid State Phys. **21**, L209 (1988).
[8] A. B. Fowler, A. Hartstein, and R. A. Webb, Phys. Rev. Lett. **48**, 196 (1982).
[9] C. M. Marcus, A. J. Rimberg, R. M. Westervelt, P. F. Hopkins, and A. C. Gossard, Phys. Rev. Lett. **69**, 506 (1992).
[10] S. Datta, *Electronic Transport in Mesoscopic Systems* (Cambridge University Press, Cambridge, UK, 1997).
[11] Y. Imry and R. Landauer, Rev. Mod. Phys. **71**, 306 (1999).
[12] K. E. Aidala, R. E. Parrott, T. Kramer, E. J. Heller, R. M. Westervelt, M. P. Hanson, and A. C. Gossard, Nat. Phys. **3**, 464 (2007).
[13] M. A. Topinka, B. J. LeRoy, S. E. J. Shaw, E. J. Heller, R. M. Westervelt, K. D. Maranowski, and A. C. Gossard, Science **289**, 2323 (2000).
[14] M. A. Topinka, B. J. LeRoy, R. M. Westervelt, S. E. J. Shaw, R. Fleischmann, E. J. Heller, K. D. Maranowski, and A. C. Gossard, Nature (London) **410**, 183 (2001).
[15] T. Kramer, E. J. Heller, and R. E. Parrott, J. Phys.: Conf. Ser. **99**, 012010 (2008).
[16] B. Szafran, Phys. Rev. B **84**, 075336 (2011).
[17] C. S. Lent and D. J. Kirkner, J. Appl. Phys. **67**, 6353 (1990).
[18] Y. Wang, J. Wang, and H. Guo, Phys. Rev. B **49**, 1928 (1994).
[19] T. Ueta and Y. Miyagawa, Phys. Rev. E **86**, 026707 (2012).
[20] J. Power and G. Rawitscher, Phys. Rev. E **86**, 066707 (2012).
[21] E. Antillon, B. Wehefritz-Kaufmann, and S. Kais, Phys. Rev. E **85**, 036706 (2012).
[22] L. Nannen, Ph.D. thesis, Universität Göttingen, 2008.
[23] T. Hohage and L. Nannen, SIAM J. Numer. Anal. **47**, 972 (2009).
[24] L. Nannen and A. Schädle, Wave Motion **48**, 116 (2011).
[25] S. Rotter, J.-Z. Tang, L. Wirtz, J. Trost, and J. Burgdörfer, Phys. Rev. B **62**, 1950 (2000).
[26] L. L. Thompson and P. M. Pinsky, Int. J. Numer. Methods Eng. **38**, 371 (1995).
[27] L. L. Thompson, J. Acoust Soc. Am. **119**, 1315 (2006).
[28] J. J. Metzger, Ph.D. thesis, Max-Planck Institut f. Dynamik und Selbstorganisation, 2010.
[29] W. Bangerth, R. Hartmann, and G. Kanschat, ACM Trans. Math. Software **33**, 24/1 (2007).
[30] A. Ern and J. Guermond, *Theory and Practice of Finite Elements* (Springer, New York, 2004).
[31] G. H. Hardy, Proc. London Math. Soc. **2**, 269 (1915).
[32] P. L. Duren, *Theory of H^p spaces* (Academic, New York, 1970).
[33] S. Larsson and V. Thomee, *Partielle Differentialgleichungen und numerische Methoden* (Springer, Berlin, 2005).
[34] M. Cassé, Z. D. Kvon, G. M. Gusev, E. B. Olshanetskii, L. V. Litvin, A. V. Plotnikov, D. K. Maude, and J. C. Portal, Phys. Rev. B **62**, 2624 (2000).
[35] A. E. Hansen, S. Pedersen, A. Kristensen, C. B. Sørensen, and P. E. Lindelof, Physica E (Amsterdam) **7**, 776 (2000).
[36] B. Krafft, A. Förster, A. van der Hart, and Th. Schäpers, Physica E (Amsterdam) **9**, 635 (2001).
[37] M. Kokoreva, V. Margulis, and M. Pyataev, Physica E (Amsterdam) **43**, 1610 (2011).
[38] H. U. Baranger and A. D. Stone, Phys. Rev. B **40**, 8169 (1989).
[39] S. C. Kramer, Ph.D. thesis, Institut für Angewandte und Numerische Mathematik, Universität Göttingen, 2012.
[40] A. Jäckle and H. D. Meyer, J. Chem. Phys. **105**, 6778 (1996).
[41] A. G. Borisov and S. V. Shabanov, J. Comput. Phys. **216**, 391 (2006).